J Infrared Milli Terahz Waves (2026) 47:10
https://doi.org/10.1007/s10762-026-01118-3

RESEARCH

Design and Method of a Slow-Wave Structure based on Symmetric Grating for Traveling Wave Tube

Qinwen Xue[1] · Xuesong Yuan[1] · Zhongtao Cui[1] · Yunze Zhu[1] · Matthew Thomas Cole[2] · Yanyu Wei[1] · Yang Yan[1]

Received: 6 November 2025 / Accepted: 6 February 2026 / Published online: 12 February 2026

Abstract

Excellent performance of high-frequency structures is critical to the development of millimeter wave and terahertz traveling wave tubes (TWTs). The plane symmetric grating structure (SGS) has the advantages of large transverse dimension, simple structure and easy to manufacture with one-dimensional processing. The TM_{11} mode in SGS has characteristics of high coupling impedance and strong resonance, but its bandwidth is narrow, which limits its application in sheet beam traveling wave tube. It is found that the bandwidth of SGS can be effectively expanded by loading the coupled waveguide (operating in TE_{10} mode) in parallel with the symmetric grating in this paper. The attempt to expand the bandwidth of SGS has been done in the Ka-band. The results show that the relative bandwidth of SGS can be widened from 0.03% to 8.3%. Besides, a G-band TWT is designed, and the cross-sectional area of its slow wave structure is more than twice that of the traditional high frequency structure. The PIC simulation results demonstrate that the maximum power is 169 W at 219 GHz, corresponding to a gain of 27.2 dB, and the -3dB bandwidth is 10.5 GHz.

Keywords Symmetric grating structure · High frequency structure · Traveling wave tube · Vacuum electronics

✉ Xuesong Yuan
yuanxs@uestc.edu.cn

[1] Terahertz Radiation and Application Key Laboratory of Sichuan Province, School of Electronic Science and Engineering, University of Electronic Science and Technology of China, Chengdu 611731, China

[2] Department of Electronic and Electrical Engineering, University of Bath, Bath BA2 7AY, UK

1 Introduction

Millimeter and terahertz radiation sources have proven themselves essential in high speed communications, and phased array radar applications [1–3]. When developing higher frequency radiation sources, the size of high-frequency structures is limited due to the decreased transversal dimension, which brings difficulties in designing the electron optical systems as well as in the manufacturing and processing of the high-frequency structures [4]. Folded waveguides [5], sine waveguides [6], helix [7], microstrip meander lines [8], staggered double corrugated waveguides [9] and other structures show good performance in traveling wave tubes (TWTs). As a kind of classical slow wave structure, rectangular grating slow wave structure has many advantages, such as simplicity, large lateral size, and compatibility with planar micromachining technology, which is widely used in backward wave oscillator [10], extended interaction device [11, 12], traveling wave tube [13], diffraction radiation oscillator [14] and so on [15].

Rectangular grating slow wave structures are generally divided into double grating structures (symmetrical and staggered) and single grating structures [11–17]. This paper mainly discusses the symmetric double grating structure. The common symmetric grating structure (SGS) is presented in Fig. 1a. According to the eigenmode solver of CST MICROWAVE STUDIO, the electric field distribution diagram of the structure can be obtained by setting the electric boundary conditions. There are two modes in the SGS, as shown in Fig. 1 (b) and (c), which respectively regarded as TE_{10} mode and TM_{11} mode. In Fig. 1b, TE_{10} mode has a large bandwidth. However, the axial electric field is distributed asymmetrically about the plane $x = 0$ [18, 19], which leads to the very low coupling impedance at the gap. It is not conducive to the beam wave interaction between electrons and electromagnetic fields. In Fig. 1c, the axial electric field is symmetrically distributed about the plane $x = 0$, and it has a very strong coupling impedance, which is beneficial to the beam wave interaction between electrons and electromagnetic fields. However, its bandwidth is very narrow, and there are few works to apply this mode to TWT at present. In [20], the researchers found that the staggered grating structure can be obtained by moving the symmetric grating in the *z-axis* direction for a certain distance, as shown in Fig. 1(d). Therefore, the electric field distribution can also change, as displayed in Fig. 1(e) and (f), that Fig. 1(e) corresponds to Fig. 1(b), and Fig. 1(f) corresponds to Fig. 1(c). A lot of research has been done on this structure. When the high-frequency structure works in the mode of Fig. 1(e) [21–23], the cutoff frequency of this mode depends on the lateral width. In other words, the size of the device operating in the fundamental mode is comparable to its operating wavelength. Besides, there is also leakage in the electron beam tunnel, which needs to be suppressed by the Bragg reflector. Moreover, when the high frequency structure works in the mode of Fig. 1(f), inevitably, the backward wave oscillation of the fundamental mode and the self-excited oscillation of the 3π point will be produced [24–26].

For the SGS in Fig. 1(c), increasing the thickness of the grating and changing the transverse dimension of the beam tunnel, the electric field distribution will

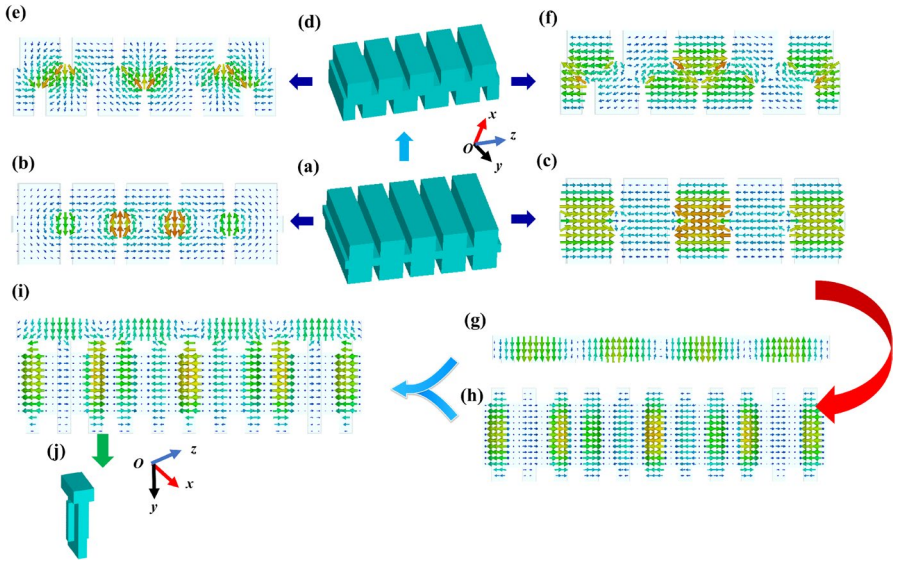

Fig. 1 The design idea diagram of the operating mode for the proposed traveling wave amplifier. **a** The five-period symmetric double-grating structure. **b** Electric field vector distribution diagram of the TE_{10} mode in the *xoz* plane of the symmetric double grating structure. **c** Electric field vector distribution diagram of the TM_{11} mode in the *xoz* plane of the symmetric double-grating structure. **d** The five-period staggered double grating structure. **e** Electric field vector distribution diagram of the TE_{10} mode in the *xoz* plane of the staggered double grating structure. **f** Electric field vector distribution diagram of the TM_{11} mode in the *xoz* plane of the staggered double-grating structure. **g** Electric field vector distribution diagram of the TE_{10} mode of the coupled waveguide. **h** Electric field vector distribution diagram of the TM_{11} mode in the *yoz* plane of the symmetric double grating structure. **i** Electric field vector distribution diagram in the *yoz* plane of the structure proposed in this paper. **j** The single-period vacuum structure proposed in this paper

not be changed. It reduces the pressure of processing technology and ensures the efficiency of beam wave interaction. Then rotate it 90 degrees along the *z-axis* and increase the number of periods to get Fig. 1(h). We use the coupling waveguide shown in Fig. 1(g) to connect in parallel with the SGS depicted in Fig. 1(h). Finally, the electric field distribution of the proposed high frequency structure is acquired, as described in Fig. 1(i). Therefore, the vacuum model of a single period for proposed TWT is shown in Fig. 1(j).

2 Beam Wave Interaction Model and Experiment Verification

According to the design idea of the slow wave structure mentioned above, the ideal mode diagram of the whole high frequency system of the proposed TWT is given below, as shown in Fig. 2. The whole circuit is mainly divided into two parts, the coupled waveguide (dark blue) and SGS (yellow).

The specific principle is described as follows. The signal is injected into the standard waveguide from port 1, entering the coupled waveguide through the

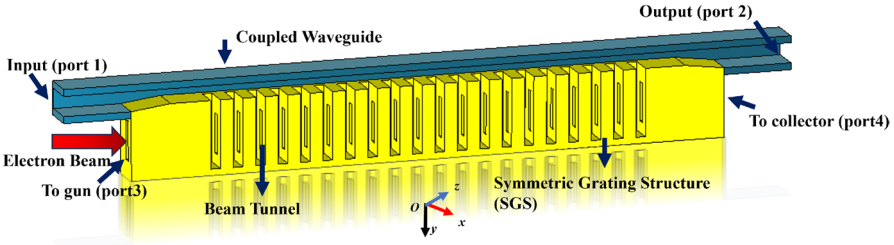

Fig. 2 Schematic of the traveling wave tube with its two main components: the symmetric grating structure (yellow) and the coupled waveguide (dark blue)

transition section. When the partial signal arrives at the coupling hole, it couples into the symmetric grating continuously. The coupled signals interact with the electron beam to obtain an amplified high frequency signal. In particular, the electron beam interacts with the RF field indirectly through gratings. Then the amplified signal is diverted to the coupled waveguide. Finally, the combined power goes out from the standard waveguide port 2.

To demonstrate the bandwidth enhancement intuitively, the eigenmode solver is employed, with periodic boundary conditions set along the z-axis, to calculate the dispersion characteristics of the single-period structure first in the *Ka*-band. As shown in Fig. 3(a), the dispersion of SGS is almost a straight line with an absolute bandwidth of 101 MHz. Furthermore, the absolute bandwidth of the single period dispersion curve obtained by expanding the coupled waveguide based on the SGS, as shown in Fig. 3(b) reaches 2.76 GHz (blue line). Let the narrow side of the coupled waveguide be denoted as m. As m increases, the bandwidth increases; as m decreases, the bandwidth decreases. It can be calculated that the relative bandwidth based on the extension of coupled waveguide has increased from 0.03% to 8.3%. At the same time, comparing the electric field distribution of the two structures inserted in the figure, we can find that they are both TM_{11}

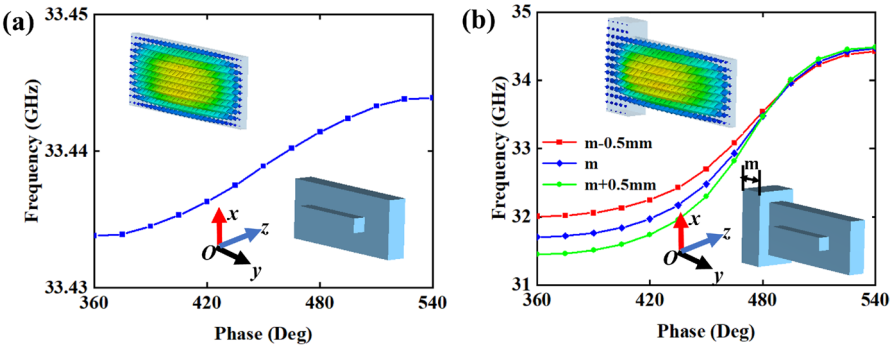

Fig. 3 Dispersion characteristics. **a** SGS in detail. Insert: Electric field distribution and single period model. **b** The structural dispersion in this paper varies with the narrow side of the coupled waveguide. Insert: Electric field distribution and single period model

mode, which proves that this method can effectively broaden the bandwidth of SGS.

Then, to verify the feasibility of the slow wave structure in TWT, we have carried out experimental research. The fabricated models are shown in Fig. 4(a). It has two parts. One is a coupled waveguide, which digs out a part component in standard waveguide *WR*−28. The other is SGS. It consists of two pieces of metal periodic grating, which is etched by machining and milling technology. Figure 4(b) shows

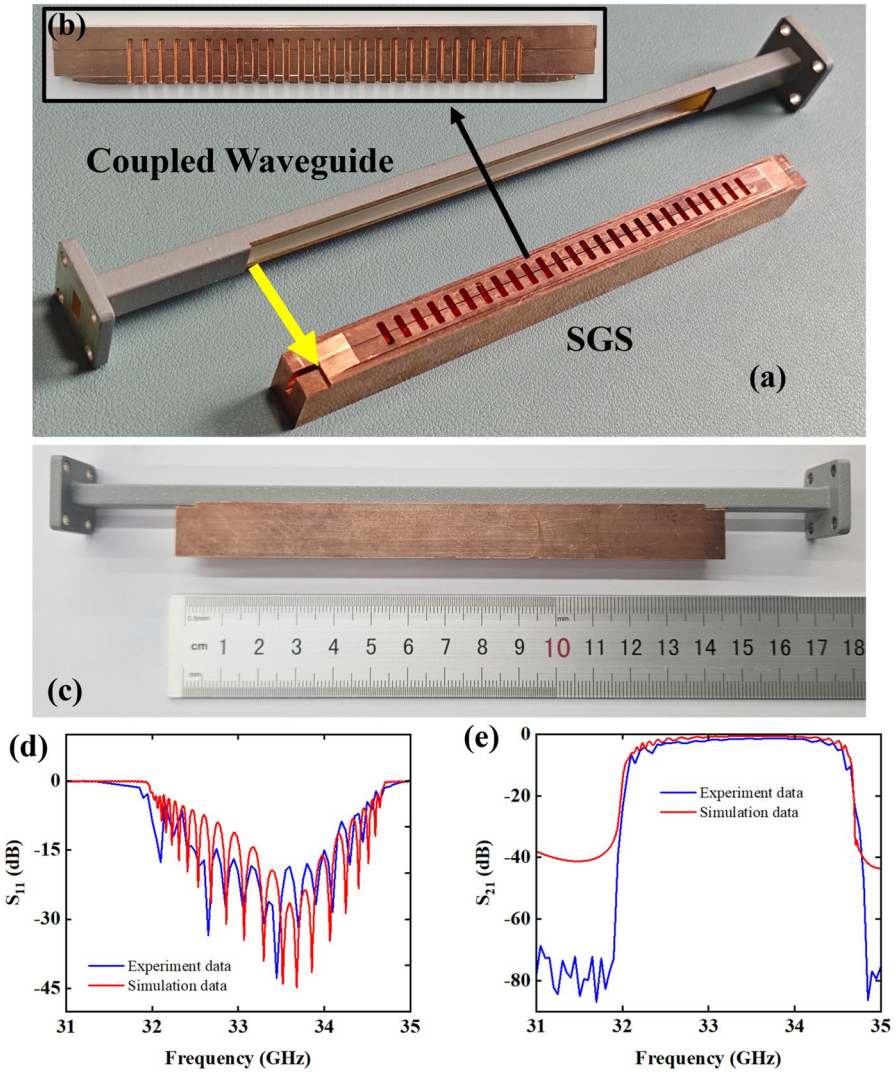

Fig. 4 Experimental verification. **a** Photograph of fabricated components. **b** One half of the SGS highlighting the grating and the coupling holes. **c** Schematic diagram of the integrated high-frequency circuit after assembly. **d** Comparison of experimental and simulated results of reflection coefficient S_{11}. **e** Comparison of experimental and simulated results of transmission coefficient S_{21}

the internal details of the SGS. It can be seen that there is a step at each end, which is designed to enable physical connection and geometric matching with the coupled waveguide. Flip the waveguide over and mount it onto the symmetric grating, then fasten it along the positions indicated by the arrows to obtain the complete model shown in Fig. 4(c).

We use a vector network analyzer (VNA, Model: AV3672C) to test the S-parameters, and the experiment results and simulation results of TWT are shown in Fig. 4. In the simulation, the time-domain solver of CST Microwave Studio was employed with electric boundary conditions set, and the lossy material selected was oxygen-free copper with an electrical conductivity of 5.8×10^7 S/m. By comparison, the resonance characteristics of S_{11} and the passband characteristics of S_{21} are in good agreement. The experimental findings demonstrate a S_{11} < -5dB, in the range of 32-34.6 GHz, and S_{21} > -3dB, in the range of 32.5-34.4 GHz, as shown in Fig. 4(d) and (e), respectively. For S_{21}, it can be found that the measured results are a little lower than the simulation results. This could be potentially explained by leaking of waves due to surface loss or the absence of welding between the parts.Therefore, it is proved that the bandwidth of SGS can be expanded by coupling waveguide through the verification experiments of processing and assembly.

2.1 Application in G-band TWT

Next, to illustrate the hot characteristics of the proposed high frequency structure, a PIC simulation of G-band TWT is conducted using CST Studio Suite [27]. Figure 5 shows a cross-sectional view of the proposed circuit. Considering the conductor loss and surface roughness in the G-band, the conductivity is set to 2.2×10^7 S/m, which is made of copper. A summary of the geometry parameters is listed in Table 1. To more intuitively demonstrate the differences between this structure and the staggered double grating structures, Fig. 6 presents a comparison of the two in terms of structural dimensions, dispersion characteristics, and average coupling impedance. Specifically, Fig. 6(a) and (c)

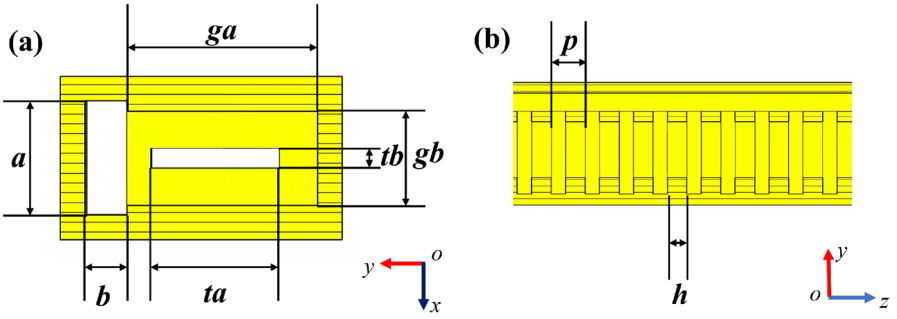

Fig. 5 Schematic diagram of the cross-section of the high frequency circuit (**a**) *xoy* plane, where *a* and *b* denote the long and short sides of the coupled waveguide, *ga* and *gb* denote the long and short sides of the grating, and ta and tb denote the long and short sides of the electron beam tunnel. (**b**) *yoz* plane, where *p* denotes the length of a single period and *h* denotes the thickness of the vane

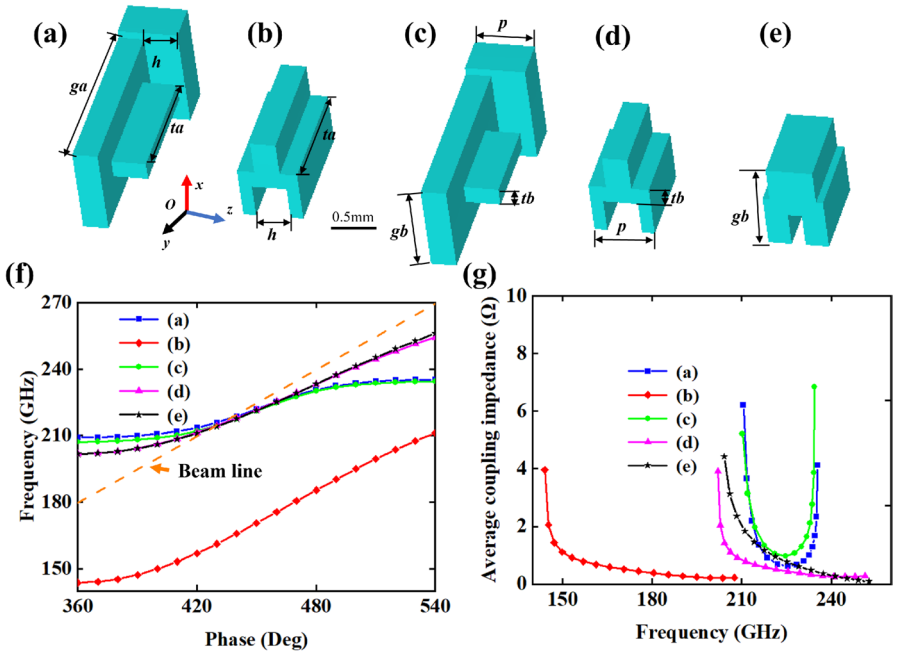

Fig. 6 Cold Characteristics. (**a**), (**c**) The slow wave structure proposed in this paper. (**b**), (**d**), and (**e**) Staggered double grating structures. Among them, the electron beam tunnels of (a) and (b) are identical in size, while those of (c), (d) and (e) are the same. (g) Comparison of dispersion characteristics. (h) Comparison of average coupling impedance

present the vacuum schematic of the single-period structure proposed in this paper, while Fig. 6(b), (d), and (e) show the single-period schematics of staggered double grating structures. Among them, the electron beam tunnels of (a) and (b) are identical in size (1.04mm × 0.16mm), while those of (c), (d) and (e) are the same(0.74mm × 0.16mm). The vane thickness $h = 0.3$mm of (a), (b), (c) and (d) is consistent. The vane thickness of (e) is 0.12mm, and the single-period length p and gb of all structures are the same. Figure 6(f) depicts the dispersion characteristics of all single-period structures, where the dashed line represents the synchronous voltage line, while Fig. 6(g) presents the comparison curves of their average coupling impedance. It can be seen that: first, the structural dimensions can be doubled; second, the coupling impedance is relatively high, whether compared under the condition of the same vanes in (a) and (b) or under the condition of electron beam tunnels with the same size in (c), (d) and (e). Although the bandwidth of this structure is relatively narrow, the thicker vanes are more conducive to reducing the machining difficulty and solving the heat dissipation problem. A higher coupling impedance is favorable for the sufficient interaction between the high-frequency field and the electron beam.

Figure 7 shows the S-parameter of the TWT. Port 1 is input and port 2 is output. Port 3 is set at the emission end of the electron beam tunnel, and port 4 is set at the end. The dimensions of Port 3 and Port 4 match those of the electron beam tunnel,

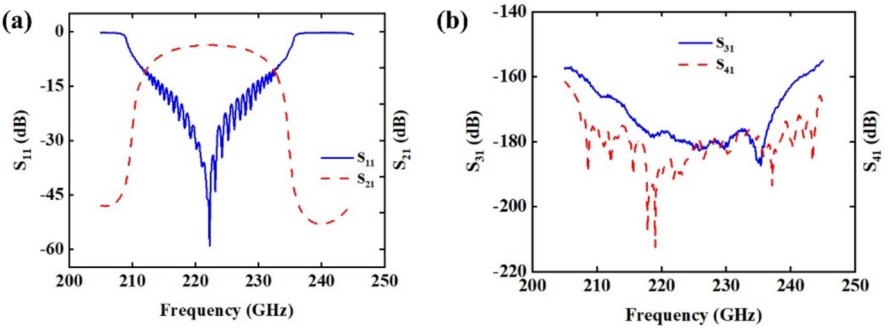

Fig. 7 Schematic diagram of S-parameter. **a** S_{11} and S_{21}. **b** S_{31} and S_{41}

which is $ta \times tb$. S_{11} is lower than -15 dB from 214 to 230 GHz. S_{31}, and S_{41} are both below -155dB.

The circuit operates at the forward + 1st spatial harmonic. To test the amplifier in high current density, a sheet beam is adopted. The hot performance of the TWT is simulated. The operating voltage was set to 26.8 kV, the current is 0.3 A, the cross-sectional area of beam is 0.7×0.1 mm, the current density is 428 A/cm^2, the number of pitches is 62, and the total length of the beam tunnel is 32.9 mm, and the

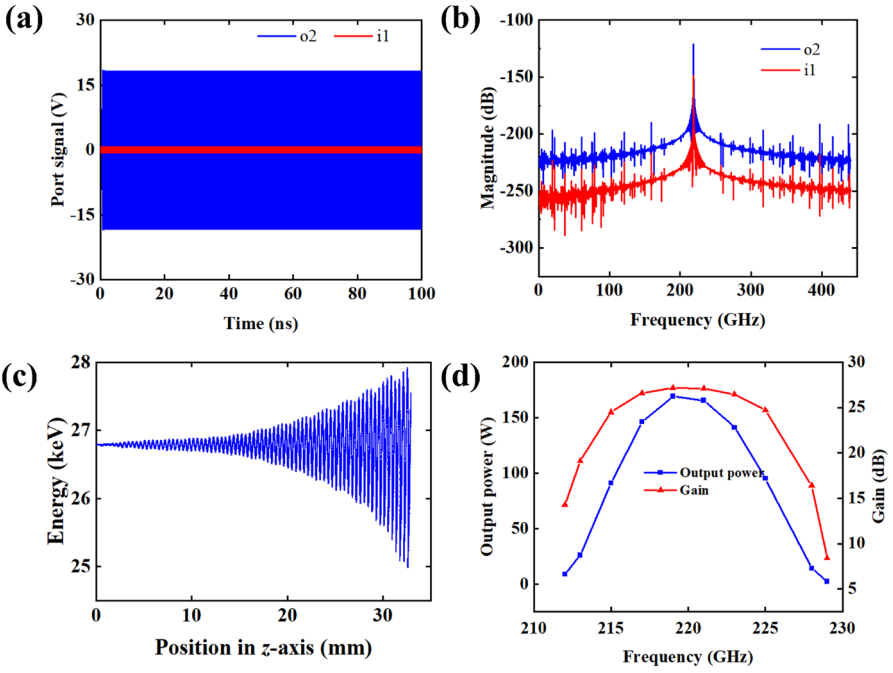

Fig. 8 TWT performance. **a** Input and Output signals at 219 GHz. **b** Spectrum diagram. **c** Phase space diagram. **d** Output power and gain

longitudinal magnetic field is 0.55 T. As shown in Fig. 8(a), when the input signal is 0.32 W, the maximum power obtained at the frequency of 219 GHz is 169 W. Figure 8(b) shows the Fourier transform of the frequency spectrum at 219 GHz. Note the absence of any parasitic components. The gain of the output signal is 27.2dB and the gain per unit length of the beam tunnel translates to 8.45dB/cm. Figure 8(c) depicts the phase space diagram. It can be observed that the maximum electron energy reaches 27.9 keV and the minimum electron energy is 25 keV. This indicates that the energy the high-frequency field gains from the electron beam is greater than the energy the electron beam absorbs from the high-frequency field, thereby enabling the amplification of the input signal. Figure 8(d) describes the variation of the gain and output Table 1 power with frequency. The −3dB bandwidth is 10.5 GHz.

To observe the energy transmission, the Poynting vector at the operating frequency of 219 GHz (maximum output power frequency point) is monitored. Figure 9(a) shows the energy flow density distribution. After the electron beam interacts with the modes in the grating, the amplified signal is continuously coupled into the waveguide through the coupling hole and superimposed, and finally output from the waveguide. Figure 9(b) captures the last few periods of Fig. 9(a). It can be seen that the signal is amplified. Figure 9(c) is the cross-sectional view of vacuum model of TWT. The standard waveguide *WR*−4 is used at the input and output ports. There is an integral surface set at the junction of coupled waveguide and SGS, marked by the dotted line. The surface integral of the Poynting vector is calculated. The normal vectors of all integral surfaces are in the *y* direction. The instantaneous power change relationship as a function of time is shown in Fig. 9(d). The green line represents the result of integration from the S_1 (the 56th period), the red represents the result of integration from the S_2 (the last period), and the blue represents the sum of integration S_{total} of all faces. It can be seen from the Fig. 9(d) that the power at S_2 is greater than that at S_1, indicating that the energy change trend in the symmetrical grating is consistent with that in the coupled waveguide. It can be seen from Fig. 9(e) that the average power in Fig. 8(a) is consistent with the value calculated from the integrated surface S_{total}. It is verified that the power is exchanged along the *y-axis*. That is to say, the coupled signal in the symmetric grating interacts with the electron beam and excites a high frequency field, continuously feeding the coupled waveguide for superposition.

Table 1 Parameters of structure

Symbol	Description	Value(mm)
tb	Narrow side of beam tunnel	0.16
h	Thickness of the vane	0.3
b	Narrow side of coupled waveguide	0.34
p	Period	0.52
gb	Narrow side of grating	0.78
a	Long side of coupled waveguide	0.92
ta	Broad side of beam tunnel	1.04
ga	Long side of grating	1.54

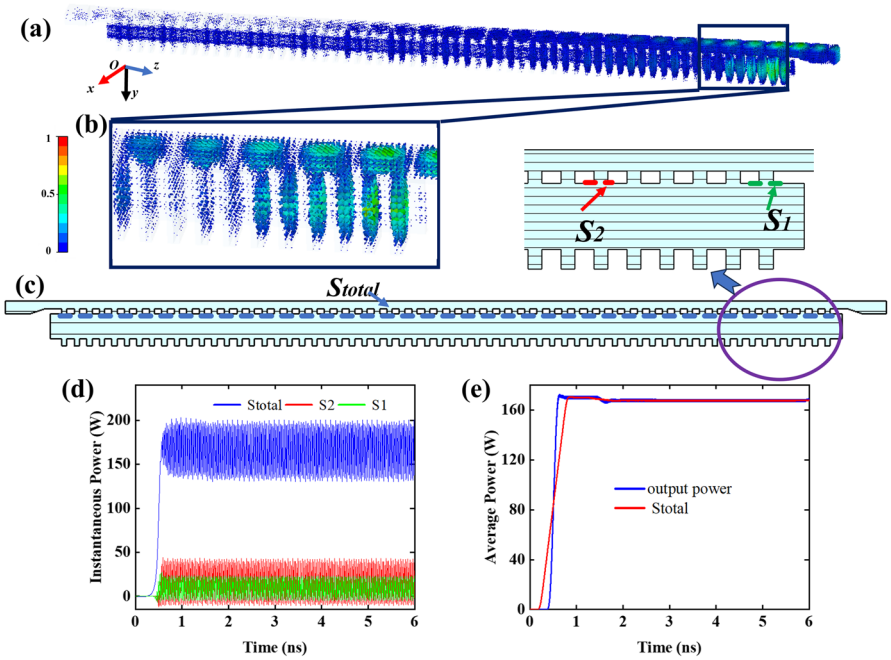

Fig. 9 Schematic diagram of power flow at 219 GHz. **a** Power flow. **b** In detail. **c** Vacuum model of TWT. **d** Poynting vector integrated over S_{total}, S_1 and S_2. **e** Comparison between the output port power o2 and the power calculated from the integrated surface S_{total}

3 Conclusion

A method for expanding the bandwidth of SGS to develop millimeter wave and terahertz TWTs is proposed in this paper, which is verified by experiments. The SGS connected in parallel with the coupled waveguide realises the traveling wave amplification, which shows good performance application in G-band TWT. PIC simulation results demonstrate that the advantages of the modelled device are as follows. Firstly, the cross-sectional area of the proposed structure (0.92×1.88 (i.e. $a^*(ga+b)$)) has been increased by a factor of 4.67, compared with the standard $WR-3$ waveguide (0.86×0.43mm). The thickness of the grating with the same length of single period in the SGS is 2–3 times that of staggered double slow wave structure. It improves the mechanical strength of the structure in terahertz TWT. Secondly, because it is extended on the basis of a rectangular waveguide, it does not need any complicated input and output structures for ultra-wideband traveling wave signal high-frequency system. Thirdly, compared with the single-grating structure, this structure can operate at a lower voltage with a wide operating bandwidth. Furthermore, symmetric gratings can be loaded simultaneously on both sides of the waveguide E-plane. And by loading waveguides on both sides of the symmetric dual gratings, bilateral reverse coupling and forward coupling can be achieved, which further increases the size of the high-frequency structure.

Acknowledgements This work was supported by the Natural Science Foundation of Sichuan Province under Grant 2024NSFSC0467 and National Natural Science Foundation of China under Grant 61771096.

Authors Contributions Qinwen Xue: Data curation (equal); Investigation (equal); Writing -original draft (equal). Xuesong Yuan: Conceptualization (equal); Funding acquisition (equal); Investigation (equal); Writing—review &editing (equal). Zhongtao Cui: Investigation (equal). Yunze Zhu: Data curation (equal). Investigation (equal). Matthew Thomas Cole: Writing-review & editing (equal). Yanyu Wei: Investigation (equal). Yang Yan: Investigation (lead).

Data Availability No datasets were generated or analysed during the current study.

Declarations

Ethical Approval Not applicable.

Competing interests The authors declare no competing interests.

References

1. Qu B, Li Z, Zhao S, et al.: Design and Experimental Study of an E-Band CW Space TWT. IEEE Trans. on Plasma Science **51**(4), 1059-1064 (2023)
2. Huang Y, Shen Y, Wang J.: From terahertz imaging to terahertz wireless communications. Engineering **22**(3), 106-124 (2023)
3. C. Paoloni et. al.: Horizon 2020 TWEETHER project for W-band high data rate wireless communications. In: Proc. IEEE Int. Vac. Electron. Conf. (IVEC), pp. 1–2. Beijing, China, (2015)
4. J. H. Booske. : Vacuum electronic high power terahertz sources. IEEE Trans. Terahertz Sci. Technol. **1**(1), 54-75 (2011)
5. Li F, Xiao L, Ma T, et al. Demonstration of W-Band 30-W Continuous-Wave Folded Waveguide Traveling Wave Tube with Lowered Operation Voltage and Improved Gain Flatness. Journal of Infrared Millimeter and Terahertz Waves **41**(10), 1252 - 1266 (2020)
6. Luo J et al.: Design and Analysis of a 0.33-THz Sine-Shaped Folded Waveguide Traveling Wave Tube. IEEE Trans. on Electron Devices, **70**(6), 2814–2820 (2023)
7. Dong J et al.: Experimental Investigation of a Q-Band Helix Traveling-Wave Tube With High Efficiency. IEEE Trans. on Electron Devices **71**(1), 846-852 (2024)
8. Shen F, et al.: "Symmetric Double V-Shaped Microstrip Meander-Line Slow-Wave Structure for W-Band Traveling-Wave Tube," IEEE Trans. Electron Devices, **59**(5), 1551-1557, (2012).
9. Field M, Kimura T, Atkinson J, et al.: Development of a 100-W 200-GHz High Bandwidth mm-Wave Amplifier. IEEE Trans. Electron Devices, **65**(6), 2122-2128 (2018)
10. A. Jameel et al.: Design, Simulation, and Cold Test of a W-Band Radial Rectangular Concentric Grating Backward Wave Oscillator. IEEE Trans. Electron Devices, **71**(6), 3895-3901, (2024).
11. Zhang T, Niu X, Liu Y, et al.: Design and Experiment of a Sheet Beam Gun for Extended Interaction Oscillator. Journal of Infrared Millimeter and Terahertz Waves **45**(3-4), 171–183 (2024).
12. Chang Z, Shu G, Tian Y, et al.: A broadband extended interaction klystron based on multimode operation. IEEE Trans. Electron Devices **69**(2), 802-807 (2022)
13. Dong Y, Zhen Y, Guo J, Xu D.: A hybrid dispersion slow wave structure for 0.66 THz traveling wave tubes. IEEE Electron Device Lett. **44**(11), 1888–1891 (2023)
14. Kovalov I O, Miroshnichenko V S, Senkevich Y B.: Diffraction Radiation Oscillator with Frequency Tuning on Mutual Coupled Modes in an Open Resonant System. Progress In Electromagnetics Research C **87**(1), 1-11 (2018)
15. Yang Y, Zhang P, Zheng Y, et al.: A Method for Designing Multibeam Higher Order Mode Extended Interaction Oscillators Based on Subwavelength Hole Array Smith-Purcell Radiation. IEEE Trans. on Microwave Theory and Techniques, **73**(4), 2242–2250 (2025)
16. Earley L, Carlsten B, Krawczyk F, et al.: Wideband RF Structure for Millimeter Wave TWTs. American Institute of Physics (2006)

17. Joye C D, Calame J P, Garven M, et al.: UV-LIGA microfabrication of 220 GHz sheet beam amplifier gratings with SU-8 photoresists. Journal of Micromechanics and Microengineering **20**(12), 125016 (2010)
18. Zhang Y, Gong Y, Wang Z, et al.: Study of High-Power Ka-Band Rectangular Double-Grating Sheet Beam BWO. IEEE Trans. on Plasma Science **42**(6), 1502-1508 (2014)
19. Carlsten, Bruce E.: Modal analysis and gain calculations for a sheet electron beam in a ridged waveguide slow-wave structure. Phys. Plasmas **9**(12), 5088-5096 (2002)
20. Shin Y M, Barnett L R, Luhmann N C.: Phase-Shifted Traveling-Wave-Tube Circuit for Ultrawideband High-Power Submillimeter-Wave Generation. IEEE Trans. on Electron Devices **56**(5), 706-712 (2009)
21. Zhao C, Xu H.: A Modified Double Staggered Grating Waveguide Slow Wave Structure for Sub-THz Traveling Wave Tubes. IEEE Trans. on Electron Devices **70**(6), 2746-2752 (2023)
22. G. Shu.: Dispersion and Dielectric Attenuation Properties of a Wideband Double-Staggered Grating Waveguide for Subterahertz Sheet-Beam Traveling-Wave Amplifiers. IEEE Trans. on Electron Devices **68**(11), 5826–5833 (2021)
23. Shu G, Liao J, Ren J, et al.: Study of a 0.3 THz Double-Staggered Grating Waveguide-Based Band-Edge Oscillator. IEEE Trans. on Electron Devices **52**(10), 5151–5158 (2024)
24. Wang J, Shu G, Liu G, et al.: Ultrawideband coalesced-mode operation for a sheet-beam traveling-wave tube. IEEE Trans. Electron Devices **63**(1), 504-511 (2016)
25. Wan Y, Wang J, Liu Z, et al.: The High-Order Coalesced TM11-Like Mode Operation for 220 GHz Sheet Beam Traveling-Wave Tube. IEEE Transactions on Terahertz Science and Technology **11**(2), 159-164 (2021)
26. Cui Z, Yuan X, Xue Q, et al.: Theoretical research on a large beam tunnel, coalesced-mode broadband traveling wave tube. Phys. Plasmas **31**(12), 1059-1064 (2024)
27. CST. CST MWS and PS Tutorials. [Online]. Available: http://www.cst.com. Accessed 19 Jan 2026